In multi electron beam systems, "Neighbours Matter"

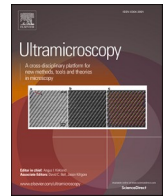Mohammadi-Gheidari, A.; Kieft, E. R.; Guo, X.; Wisse, M.; Kruit, P.

Important note
To cite this publication, please use the final published version (if applicable).
Please check the document version above.

In multi electron beam systems, "Neighbours Matter"

A. Mohammadi-Gheidari [a,b,*], E.R. Kieft [b], X. Guo [a], M. Wisse [a], P. Kruit [a]

[a] *Faculty of Applied Sciences, Delft University of Technology, Lorentzweg 1, 2628CJ Delft, the Netherlands*
[b] *Thermo-Fisher Scientific, De Schakel 2, 5651 GG Eindhoven, the Netherlands*

ARTICLE INFO

ABSTRACT

In the Multi beam source (MBS) of our Multi Beam Scanning Electron Microscope (MBSEM), an aperture lens array (ALA) splits the emission cone of the Schottky field emitter into multiple beamlets. When the apertures in the ALA are close to each other, the ALA can introduce aberrations to these beamlets through the electrostatic interaction of neighbouring apertures with each aperture's lens field. When the apertures are arranged in a square grid pattern, the aberration causes fourfold astigmatism. The effect on the beam spot is analyzed through a combination of 3D simulations and experimental validation. To counterbalance the fourfold astigmatism, a correction scheme is proposed in which a slightly non-round profile is applied to the aperture lenses.

1. Introduction

1.1. The MBSEM

Present SEMs equipped with a high brightness Schottky electron source can achieve sub-nanometer resolution with a typical probe current of tens to hundreds of picoamperes (pA). This probe is scanned across the surface of a sample for a typical scanning area, known as "field of view" (FoV), in the order of tens of μm^2. For imaging of samples with a larger total area of mm^2 or more such as the whole surface of a wafer in semiconductor industry, or for 3D slicing and imaging of biological samples, the throughput of current SEMs is unsatisfactory. One of the limiting factors to the throughput is the low probe current which is the consequence of the limited (reduced) brightness of the electron source. To enhance the throughput, while keeping the resolution unaffected, one option is to use "Multi beam technology" where the number of focused beams in the column is increased. To this end, Multi Beam Scanning Electron Microscopes (MBSEM) have been developed by Zeiss [1] and at Delft University of Technology [2–7]. We limit our discussion to the latter, in which the source delivers a square array of 14×14 (196) focused beams onto a sample simultaneously with a resolution and current per beam comparable to those of a state-of-the-art single beam SEM [2–4]. A very brief description of the electron optical working principle of the MBSEM is given here, and more detailed information is presented elsewhere [2–4]. The system consists of a commercially available Nova-Nano-SEM 200 column from FEI (nowadays part of Thermo-Fisher) equipped with a novel multi-electron beam source

(MBS) module (see Fig. 1).

The beams from the source are collimated into the SEM column by an accelerator lens (ACC). In order to avoid chromatic dispersion, the multiple images of the source are positioned in the object principal plane of this lens. The ACC creates a first common crossover of all the beams which is further imaged by the C2 lens onto the variable beam limiting aperture (VA) where the opening angle of the beams is defined. The intermediate magnetic lens (INT) is used to image the VA (thus common crossover of the beams) onto the coma free plane of the high resolution (HR)/ultrahigh resolution (UHR) objective lens. There is a large demagnification (from 90 nm to a sub-1 nm geometric source image) from the MBS image plane towards the sample plane. One of the essential components of the MBSEM is the MBS [8,9] which produces an array of focused beams for the rest of the electron optical column of the MBSEM. The MBS (see Fig. 2) is composed of the electron source unit, two macro-electrodes (E-1 and E-2) and an array of micro-apertures on a thin silicon membrane, fabricated using MEMS fabrication technology. These micro-apertures play a double role: 1) they split the solid emission cone of the high brightness Schottky electron source into an array of beams and 2) in combination with the two macro-electrodes they focus the different beams onto the MBS image plane; in other words, they act as a low-aberration aperture lens array (ALA).

1.2. Enlarged beam size due to fourfold astigmatism (Octupole effect)

In the original applications of the MBSEM, we concentrated on the highest resolution [2–4]. To achieve a high resolution, a relatively low

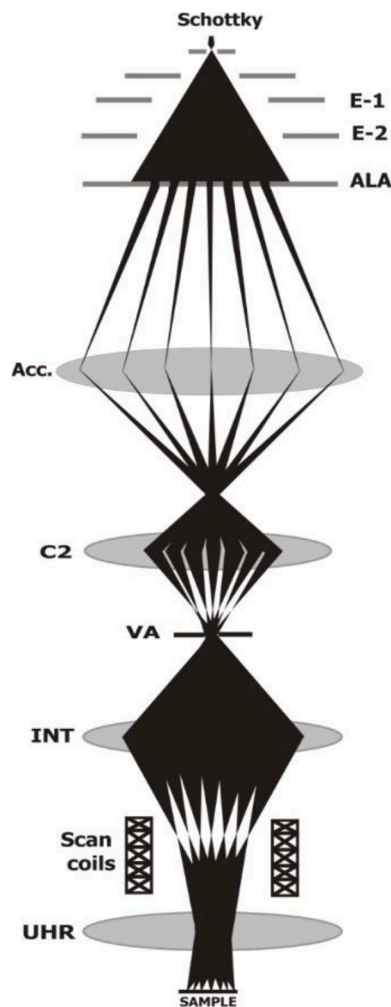**Fig. 1.** Schematic overview of electron optical configuration of the MBSEM with the multi beam source (containing the Schottky electron source, electrode 1, electrode 2, and the aperture lens array abbreviated as E-1, E-2, and ALA, respectively), an accelerating lens (ACC), a condenser lens (C2), a variable aperture mechanism (VA), an intermediate lens (INT), scanning coils, and high and ultrahigh resolution objective lenses (HR/UHR).

beam current of only tens of picoamperes (pA) per beam is used. That is, most of the current transmitted through the ALA is stopped by the VA and only a small fraction contributes to the final probe. It should be noted that experimentally measured electron optical performance of the

MBSEM in this configuration was found to be in a perfect agreement with theoretical predictions [2–4]. Recently, however, the electron optical performance of the MBSEM was re-evaluated for a higher probe current regime with a current of about 1 nA per beam. In the MBSEM the probe current can be increased simply by choosing a larger size of the VA. The maximum achievable current can then be obtained when the VA is completely taken out of the beam path which effectively makes the micro-apertures of the ALA act as the only beam limiting apertures, one per beam. Removing the VA will naturally enlarge the sizes of the probes due to a larger contribution from the objective lens aberrations. In practice, however, it was found that as soon as the current in the beam is increased, the sizes of the spots are increased, unexpectedly, to beyond the lens aberration contributions considered previously [2–4]. The first suspicion about the cause of this was that the additional blur was the result of Coulomb interactions. After a rigorous and careful simulation and analysis, it was found however that the effect of the Coulomb interactions, though not negligible, cannot fully explain the observed spot enlargement. A closer analysis of full 3D ray tracing results revealed a four-fold astigmatism in the spots whose star-shape was only easily observable at out-of-focus planes. Because of symmetry reasons, none of the electron optical elements in the system below the MBS can contribute to four-fold astigmatism, which is caused by an octupole field component. Hence to understand its causes and its magnitude, we only need to consider the MBS, and in particular the aperture lens array. Due to the neighbouring aperture lenses in the ALA, the equipotential surfaces of every aperture lens deviate from the rotationally symmetric shapes that a plate with a single central aperture would have. Stated differently, when the different apertures in the ALA are sufficiently close together (i.e., when the ratio of holes to surrounding material is high), the fields of neighbouring aperture lenses will tend to overlap and add multipole field components to each other's otherwise rotationally symmetric profiles. These deviations of the equipotential surfaces are manifested as a multipole effect in the individual beamlets, and the degree of the multipole depends on the distribution pattern of the neighbouring apertures in the ALA membrane. In a regular, square (orthogonal) pattern of apertures as used in the MBS, fourfold astigmatism will be the dominant aberration. In fact, once the VA is no longer the final beam limiting aperture of the system, the filling factors of the micro-apertures are 100%, and higher order aberrations like the fourfold astigmatism can become important. A similar effect has previously been observed through experiments in a different setup where an orthogonally distributed array of gauze lenses was involved [11], and more recently is speculated in a micro-lens array of a multi beam system [12]. In this paper, we present an analysis of the neighbouring aperture effect based on the full 3D simulations as well as experimental data. Moreover, we propose a method to eliminate the effect.
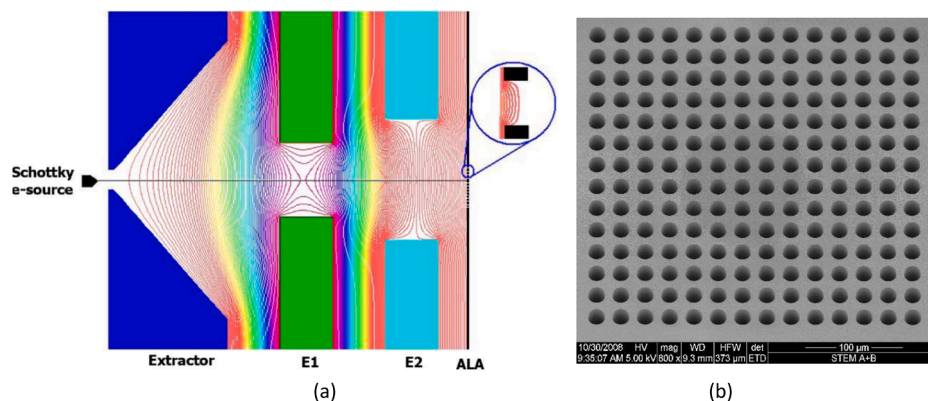
Fig. 2. Panel a, MBS configuration, with its equipotential lines as modeled by the EOD program [10]. The inset picture of panel a demonstrates how a micro-aperture lens is created. Panel b, SEM image of the 14×14 micro-aperture lens array with 15 μm diameter and 20 μm pitch, distributed orthogonally on a silicon membrane.
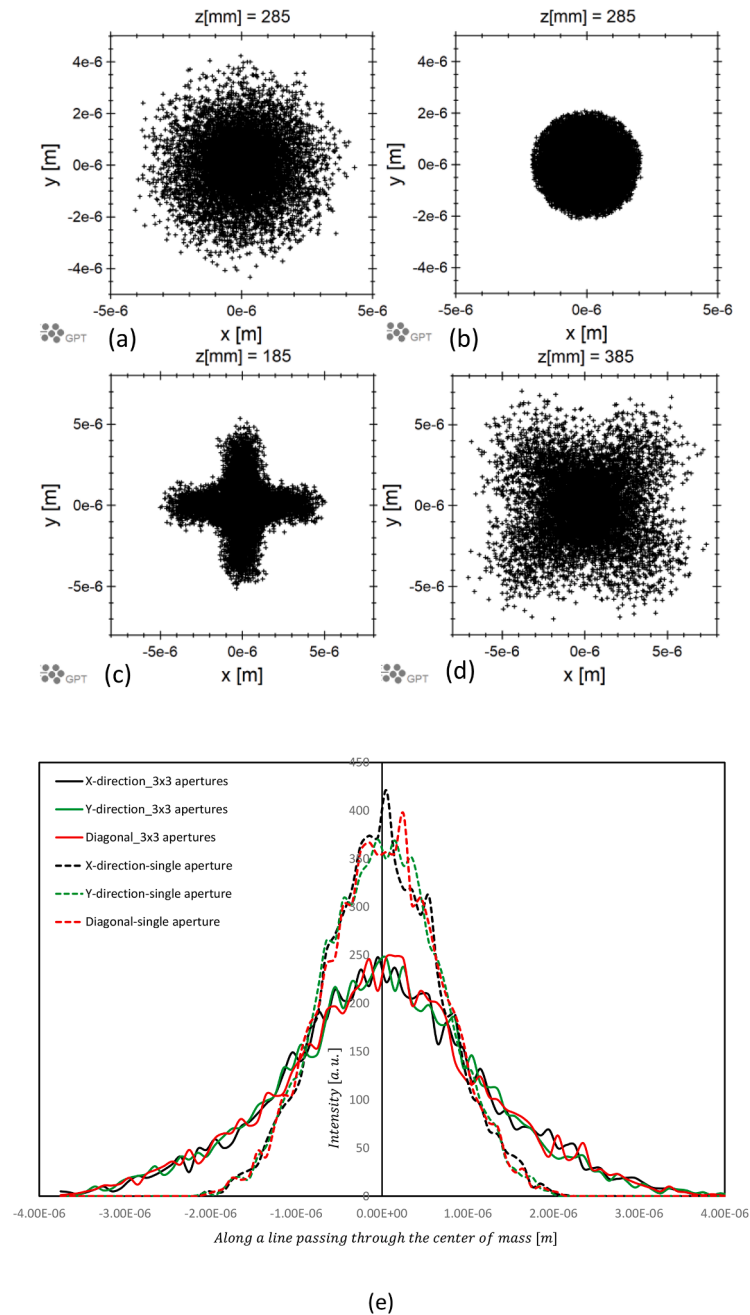
Fig. 3. Spot profile for a micro-aperture lens: a) with eight neighboring aperture lenses; b) where all the neighboring aperture lenses have been removed; c) at a plane $\Delta z = 100$ mm before the MBS image plane; d) at a plane $\Delta z = 100$ mm after the MBS image plane; e) the 1D intensity profiles of the spots for a and b along x, y, and diagonal directions. Notice that the scales of panels a) and b), c) and d) are the same.

2. Characterizing fourfold astigmatism in the spots

2.1. Simulation recipe

To study the octupole effect induced by the neighbouring apertures in the ALA, we have used GPT+BEM software package from Pulsar Physics [13] for both the calculation of 3D electrostatic field of the MBS and for subsequent electron tracing. The field calculations are performed using the built-in Boundary Element Method (BEM) solver where the input of the BEM solver are the discretized surfaces of all electrodes in the form of low-aspect triangles with gradual transitions in size. The output of the solver are the equivalent surface charges for each triangle for unit potential at each electrode. This numerical approach reduces the dimensionality from a 3D problem to a 2D surface problem in 3D space.

The relevant scales in the MBS vary immensely, ranging from few micrometer sizes for the micro-aperture lenses to a couple of millimeters for macro electrodes inner and outer diameters. However, the approach is relatively insensitive to scale differences making it a very good match for small structures such as micro-apertures in a much larger overall geometry. Once the fields are computed using BEM, the GPT code tracks sample trajectories using a 5th order Runge-Kutta solver with adaptive stepwise control from source to target plane. Optionally included are 3D macroscopic and microscopic Coulomb interactions between the electrons but for all of the simulations here this option has been switched off. In the presented simulation we use an angular precision for the surface triangles of 5° which has been verified to give stable results. Although not impossible, having all the aperture lenses in the ALA makes the field calculation computationally intensive and take considerable time on our
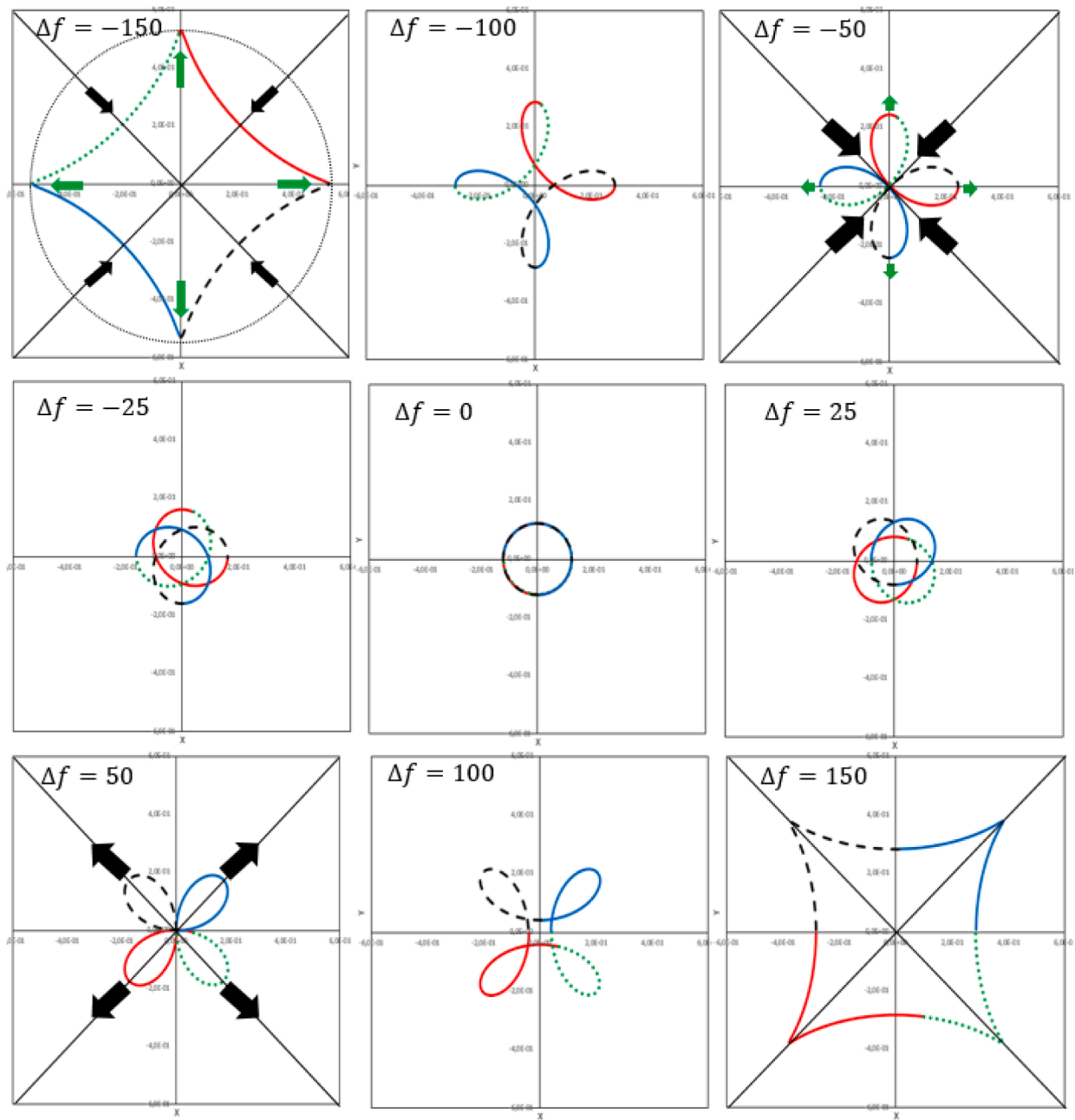
Fig. 4. Shape of a circular beam at various planes after a combined octupole field and an (ideal) aperture lens.

parallel computing infrastructure. With 30 cores it takes almost a week to calculate the field and trace 100 K particles. We therefore had to accept only simulating a subset of 3 × 3 apertures in the ALA, and tracing particles only through the central aperture in this simplified ALA. With 30 cores it now takes almost two days to calculate the field and trace 100 K particles. The 3 × 3 array is chosen because the central aperture will have all the usual 8 neighbouring apertures and can thus be used to check octupole as well as higher order aberrations induced by the neighbours. In addition, tracing electrons only through the central aperture will make sure the beam is free from off-axial aberrations that might complicate the analysis.

2.2. Simulation results

The apertures in the ALA have a diameter of 15 μm and are distributed orthogonally with a pitch of 20 μm on a (thinned) silicon wafer of 10 μm thickness. The (nominal) electric field on the surface of the ALA plate is 2.13 kV/mm. The electron energy on the ALA and MBS image plane (screen) is 5 keV. The (fixed) distance between the electron source and ALA is about 13 mm and the (fixed) distance between ALA and the MBS image plane is 272 mm. From first order simulation, the magnification from emitter to the MBS image plane is found to be ≈32x. With a virtual source (FW50) size of 50 nm for the Schottky source, the geometric (FW50) size of the spots at the MBS image plane is 1.6 μm.

The axial FW50 probe size, $d_{p-axial}$, containing 50% of the total probe current is calculated to be 1.76μm using the RPS algorithm [14] as follows:

$$d_{p-axial} = \left\{ \left[d_{geo.}^{1.3} + \left(d_\lambda^4 + d_s^4 \right)^{1.3/4} \right]^{2/1.3} + d_c^2 \right\}^{1/2} \tag{1}$$

Where $d_{geo.}(= 1.6\mu m)$, $d_\lambda(= 0.34\mu m)$, $d_s(= 15nm)$ and $d_c(= 24nm)$ are the FW50 contributions to the probe size of source image, diffraction,
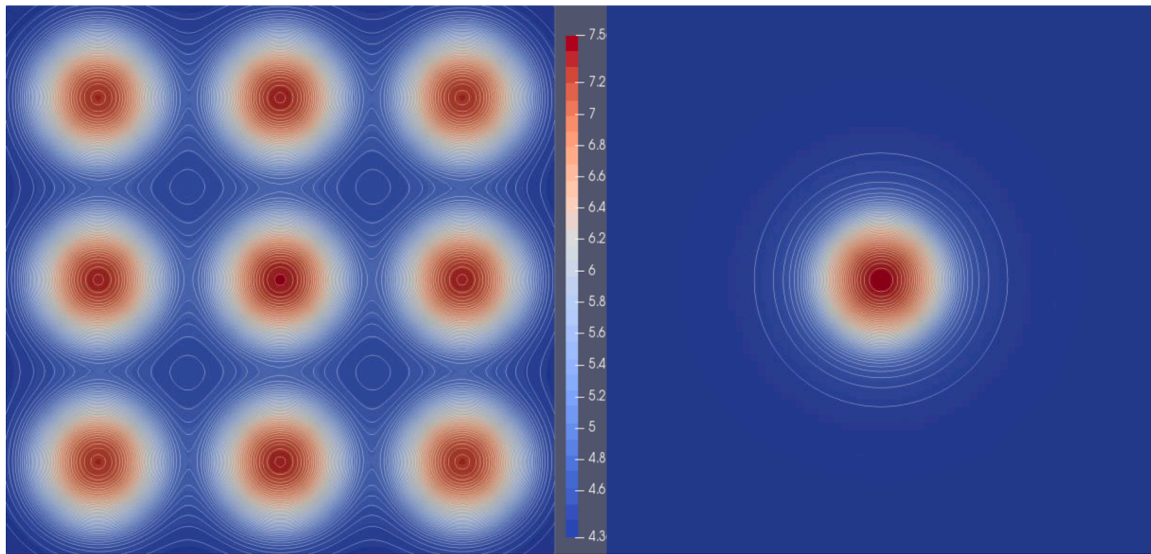
Fig. 5. Equipotential lines in plane located 2 μm above the ALA for: a) ALA with eight neighboring aperture lenses (left hand); b) where all the neighboring aperture lenses have been removed (right hand). Note that the numbers on the colored scale bar indicates the variation of potential at that plane w.r.t potential at the ALA plane (e.g., 4.5 means VALA (5000 V)+4.5 V).

spherical aberration and chromatic aberration, respectively. Fig. 3 shows the simulated spot profile, represented by the x, y positions of rays crossing the plane of interest, for two different configurations of aperture lenses in the ALA. Fig. 3a shows the spot profile recorded at the MBS image plane for an axial (central) aperture lens with eight neighbouring aperture lenses. Fig. 3b shows the spot profile recorded at the MBS image plane for the same aperture lens where all the neighboring aperture lenses have been removed. First, it is clear from Fig. 3a that the

fourfold shape of the octupole aberration is not obvious and the spot looks quite round in the MBS image plane where the beams are focused. Rather, a large spread in the spot is visible. To further illustrate this claim, the intensity profiles of the spots for Fig. 3a and Fig. 3b along three main directions, X, Y, and diagonal, are shown in Fig. 3e. Fourfold astigmatism enlarges the size of the focused spot and spreads the beam more towards the tails. The FW50 size of the spot in Fig. 3b is only 1.6 μm, whereas in Fig. 3a it is enlarged to 2.6 μm due to the fourfold
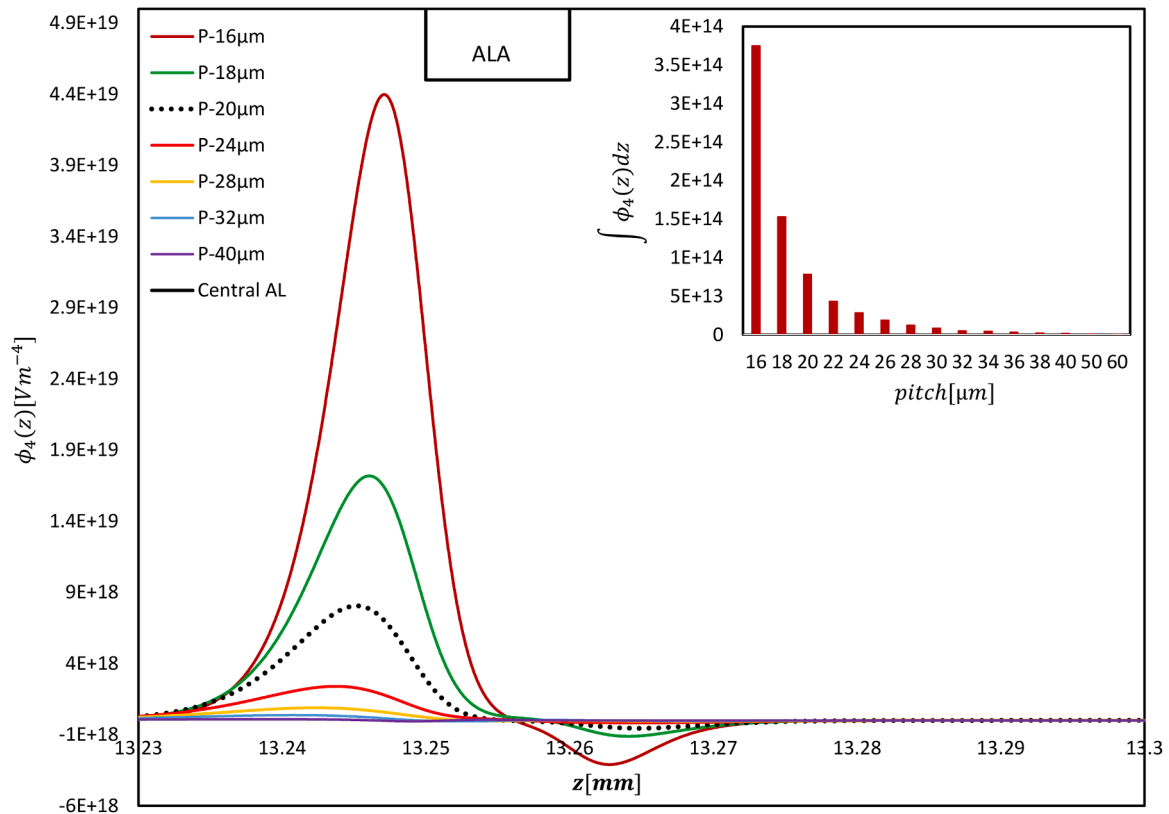
Fig. 6. The octupole characteristic function, $\phi_4(z)[Vm^{-4}]$ for different values of pitch. The inset figure gives the area under the curve of $\int \phi_4(z)dz$ for different values of pitch.
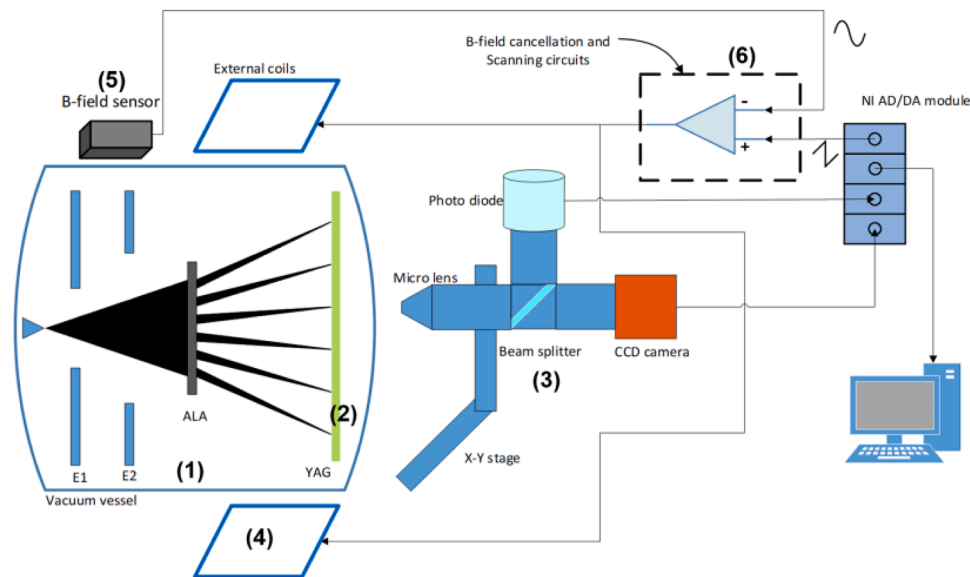
Fig. 7. Schematic overview of the experiment setup used for the measurement of spot sizes and fourfold astigmatism effect in a MBS. Shown are the MBS itself (1); a YAG screen with metal grids coated on its surface (2); an optical recording system containing a zoom (optical) lens, a beam splitter, a CCD Camera, a photodiode (3); a beam scanning unit for scanning the multiple beams across the metal grid on the YAG screen (4), and a magnetic field sensor for measuring stray field (5).

astigmatism. Since the contribution from spherical aberration is negligible, the octupole aberration induced by the neighboring apertures is found to be a dominant aberration contribution; it enlarges the FW50 spot size of the beams by a factor of ≈1.6x, in this specific example. To reveal the fourfold shape in the beam, the spot profiles are also shown at positions displaced by $\Delta z = 100$ mm before and after the focus plane, in Fig. 3c and d, respectively. These two figures show that the (fourfold) star shape "flips" its direction by 45° between planes before and after the focus, similar to how the beam elongation from regular twofold astigmatism flips by 90° after a beam crossover. To explain this "flipping" effect in some more detail, Fig. 4 schematically depicts the combined effect that an octupole field and an ideal aperture lens have on an initially circular incoming beam. The images show the resulting beam in different defocus planes, where $\Delta f = 0$ is the image plane. Black and green arrows indicate the inward and outward deflections induced by the octupole field. On top of these, there is of course the rotationally symmetric inward focusing action from the aperture lens. As can be seen

from the figures, before the image plane ($\Delta f < 0$) the octupole deflections reinforce the lens action in diagonal directions (black arrows) whereas they weaken the lens focusing action along the x, y directions (green arrows), leading to an x, y oriented cross shape. This keeps happening until the image plane. Immediately after that ($\Delta f > 0$), the octupole still reinforces the lens deflection in the diagonal direction, but now pointing outward rather than inward, leading to a diagonally oriented cross shape.

Fig. 5 shows the equipotential lines in a plane located 2 μm above the ALA for two different configurations of the aperture lenses in the ALA. Fig. 5a shows the equipotential lines for an array of 3 × 3 apertures, whereas fig.5b shows the equipotential lines for a single (central) aperture with no neighbours. The equipotential lines with fourfold symmetry are clearly visible in the Fig. 5a whereas for a single aperture, as expected, the equipotential lines are rotationally symmetric. As indicated above, the equipotential lines shown in Fig. 5a are recorded in a plane, but in fact the Octupole effect due to the neighbours doesn't
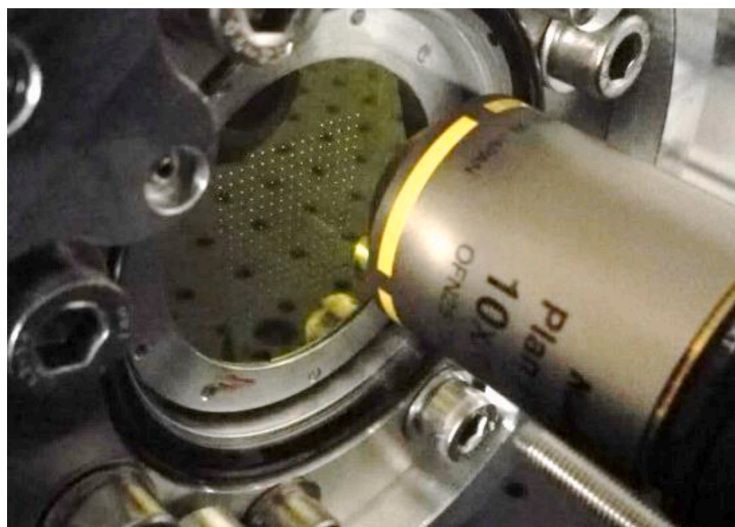
Fig. 8. Photo of the setup presented in Fig. 7, where only the YAG screen and optical (zoom) lens are shown. Note that an array of beam spots is visible on the YAG screen.
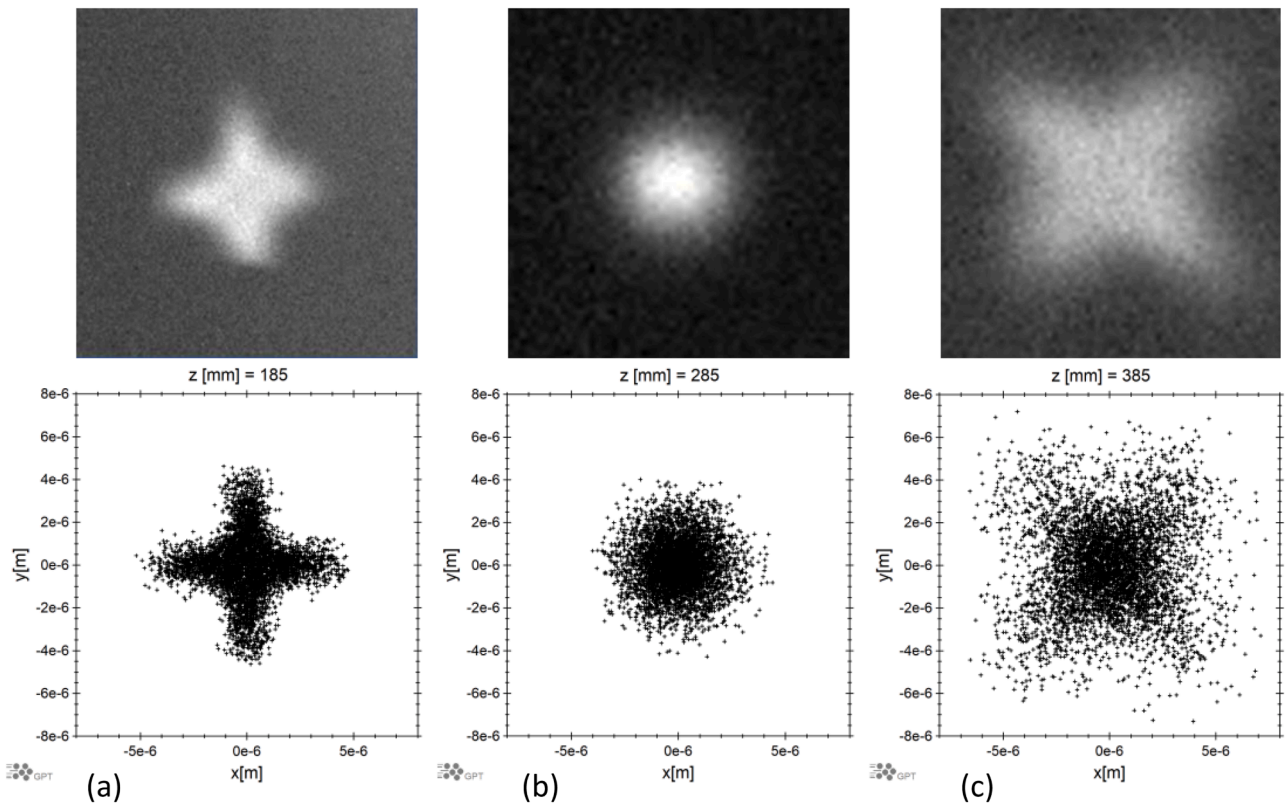
Fig. 9. Octupole aberration in an experimental MBS setup (top row). The images depict the same spot in under-focus (left), in-focus, and over-focus. In the bottom row, simulation results are shown for a qualitative comparison for different planes in a single simulation setup.

occur in a single plane but in a region along the optical axis of the aperture lens. It isn't very didactic to show the equipotential lines of all these planes. However, this can be easily shown with the octupole characteristic function, $\phi_4(z)[\mathrm{Vm}^{-4}]$.

This function is related to the actual octupole potential, in the (complex) space as $\varphi = \frac{1}{2}\phi_4(u^4 + \overline{u}^4)$, where u ($u = x + iy$) is the complex coordinate. Fig. 6 shows this function, calculated for a nominal electric field on the ALA, for different values of the pitch between apertures. The area under each graph, $\int \phi_4(z)dz$, representing the net octupole effect, is also shown in the inset figure as a function of pitch. As can be seen, the area under the graph decreases very strongly with increasing pitch. For instance, for a pitch of 30 μm the value of area under the graph drops down to an acceptable level of about 10% of its value for a pitch of 20 μm.

3. Experiment

3.1. Experiment setup

To study the octupole field effect, we mounted a copy of the MBS, containing an ALA geometry shown in Fig. 2b, in a stand-alone experimental setup. Fig. 7 shows a schematic overview of the experimental setup with its basic features. The basic features of the test setup are as follows. A YAG screen is mounted in the MBS image plane, so that the individual spots can be captured. Directly behind the YAG screen is a vacuum viewport. Outside the vacuum, an objective lens (WD=16 mm, NA=0.3) projects a magnified image of an individual spot of the array from the YAG screen, either onto a CCD camera for direct capturing of beam spot images, or onto a photodiode detector (MPPC) for the knife edge scanning method. This optical system is mounted on a linear x-y stage with 50 mm travel range in both x and y directions. The stage is driven by stepper motors. A homemade LabVIEW program controls the optical system via a controller box for automated capturing or

measurement of all spots, one at a time. For the knife edge scanning method, beam spots can be scanned across the metal grids through a set of (external) magnetic scan coils around the vacuum chamber. Moreover, these scan coils are used in combination with a magnetic measuring sensor and a dedicated negative feedback loop algorithm to cancel the electromagnetic stray fields, especially the 50 Hz EM-noise.

Fig. 8 shows a photo of part of the experiment setup, where only the YAG screen with an array of beam spots on it and the optical (zoom) lens are shown.

3.2. Experiment result

Fig. 9 shows the experimental verification of the octupole effect in under-focus, in-focus, and over-focus spots at the YAG screen. As mentioned earlier, to see the octupole effect more clearly, one should record the beam spot in a plane slightly before or after the MBS image plane respectively. Unfortunately, in the experimental setup shown in Fig. 8, this is not straightforward to do for a given configuration of the MBS, as the position of the YAG screen is fixed. Alternatively, by adjusting the voltage on the focusing electrode of the MBS (E-1) slightly, it is possible to effectively bring under- or over-focus planes to the YAG screen. In our ray tracing simulations, we found that changing the E-1 Vage value (which is nominally 25,580 V) by 1% (or ≈255 V) roughly displaces the focus by 100 mm forward or backward. Although a direct quantitative comparison of the results is not possible due to the different focus variation methods used, the dominant features are clearly visible; the experimentally obtained images show very similar patterns as in the simulation results. This confirms fourfold astigmatism as the cause of unexpected spot size enlargement in our setup.
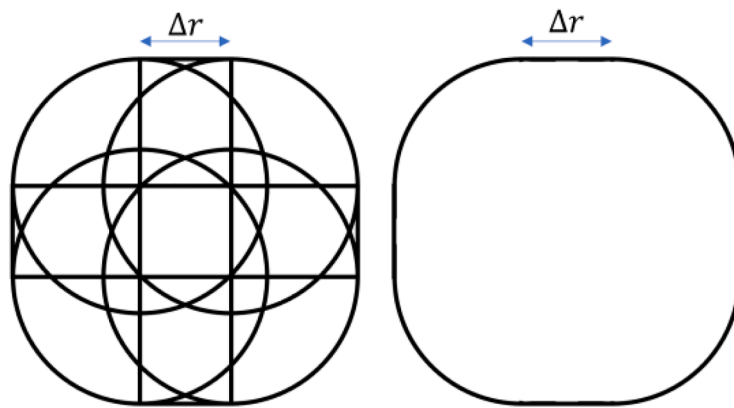
Fig. 10. Rounded square aperture and the definition of the correction parameter Δr. Note that the figure is not to scale: In reality, Δr is typically very small compared to the radius of the aperture.

4. Aberration correction

4.1 Proposed correction scheme

To correct the octupole effect of the neighbouring apertures, a counteracting octupole field in or near the same plane as the original contribution should be introduced. Two solutions have been proposed [11,12]. The solution proposed here is in essence closer to the solution proposed by Roelofs and Barth [11]. It was previously already shown that by shaping the aperture(s) of aperture lenses, one can introduce multipole components superimposed on the rotationally symmetric lens field [15]. In the MBS, a counteracting octupole field is produced by

changing the shapes of the micro-apertures from round to square with rounded corners, as shown in Fig. 10. To keep the beam currents unchanged, the areas of the rounded square apertures should remain equal to those of the regular cylindrical apertures. For a fixed field strength on the surface of the ALA, the length of the straight edges of these apertures, Δr, determines the strength of the introduced counteracting octupole field.

4.2. Simulation results
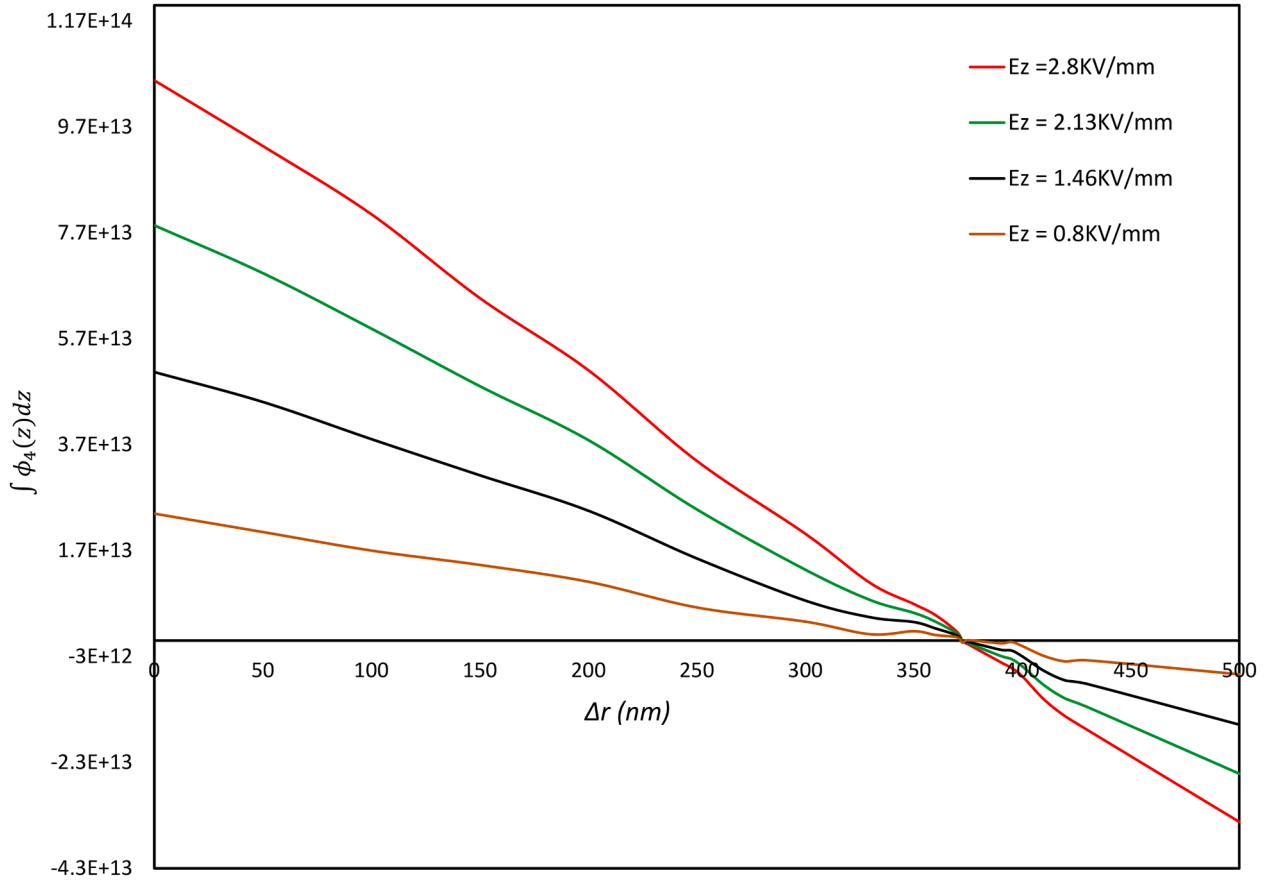
To analyze the effect of using rounded square apertures, we start with calculating the octupole field in the heart of a simplified 3×3
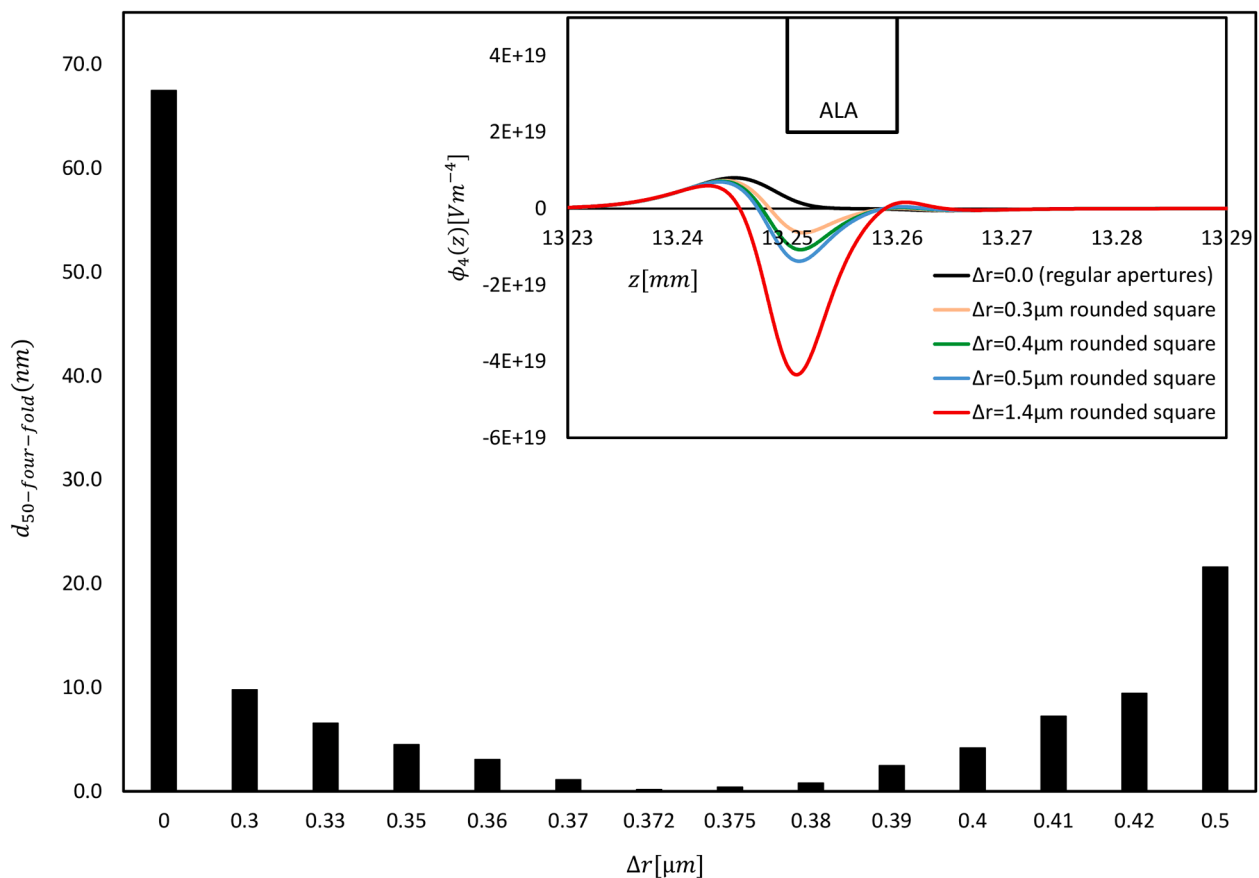
Fig. 11. FW50 size of the octupole blur for different values of Δr at the object using Eq. (2). The octupole characteristic function, $\phi_4(z)[Vm^{-4}]$ for different values of Δr is also shown in the inset figure.

Fig. 12. The area under the curve of $\phi_4(z)(\int \phi_4(z)dz)$ is shown as function of Δr for different values of electric field on the ALA. The nominal electric field on the ALA is 2.13KV/mm. For a rounded square aperture, irrespective of the electric field on the ALA, a value of $\Delta r = 0.372$ μm makes $\int \phi_4(z)dz$ equal to zero.

aperture geometry similar to the one used in Section 2. We use rounded square apertures having a range of Δr values. A quantitative method for comparing the counteracting octupole strength for different values of Δr, is to compare the FW50 value of the blur added by the fourfold astigmatism to the size of the (virtual) source. In the following, we will first derive an analytical expression for d_{FW50} for a given octupole characteristic function, $\phi_4(z)$, as introduced in Section 2.2. Then, from detailed field calculations, numerical values for $\phi_4(z)$ and d_{FW50} can be found and compared to ray tracing results.

The octupole field is a weak perturbation, and the change in the diameter of the beam while it traverses the octupole is negligible. Hence, following Newton's law, for any ray inside the beam the (extra) deflection angle caused by the octupole field can (in the non-relativistic limit) be written as

$$\delta u' = \frac{\delta p}{P} = \frac{\int eE.dt}{mV} = -\frac{2}{U}\int \frac{\partial \varphi}{\partial u} dz \tag{2}$$

where P is the momentum, E is the octupole electric field $\left(E = \frac{\partial \varphi}{\partial u}\right)$ and U is the (non-relativistic) energy of the electrons. This extra deflection causes a shift at the object of

$$\delta u = -L.\delta u' = \frac{L}{U}\int \frac{\partial \varphi}{\partial u} dz = \frac{2L}{U}\left(\int \phi_4(z)dz\right)\overline{u}^3 \tag{3}$$

where L is the (effective) distance between the object and the octupole, and u is the (complex) radius of the ray inside the octupole field. Now we define the (object-side) fourfold astigmatism coefficient A_3 by $\delta u \equiv A_3\overline{\omega}^3$, so that

$$A_3 = \frac{2L^4}{U}\int \phi_4(z)dz. \tag{4}$$

Finally, the FW50 blur at the object can be found by substituting $\overline{\omega} \rightarrow \omega_{max}/\sqrt{2}$, where ω_{max} is the (asymptotic) half cone angle of the ray filling the central aperture lens in the ALA; and equating $d_{FW50} = 2\delta u$, resulting in

$$d_{FW50} = \frac{\sqrt{2}}{2}.|A_3|.\omega_{max}^3, \tag{5}$$

with A_3 as given in Eq. (4).

Fig. 11 shows the FW50 size of the octupole blur at the object for different values of Δr. Note that the FW50 size of the (virtual) object is about 50 nm. As a reference, the inset figure gives the octupole characteristic function, $\phi_4(z)[\text{Vm}^{-4}]$ for some values of Δr.

The FW50 value of the blur calculated using Eq. (5) gives a reasonably expected result. For $\Delta r = 0.0$ μm, which corresponds to the regular aperture with eight neighbours, the calculated FW50 blur due to the octupole effect is 67 nm. If we add this blur quadratically to the (virtual) object size of 50 nm, the total object size is about 82 nm. This means the octupole effect enlarges the (virtual) object by a factor of about 1.6, which is the same factor we found through direct ray tracing and calculating the FW50 value of the spot profile in previous sections. The FW50 value of the blur decreases for increasing values of Δr up to a turning point of $\Delta r = 0.372$ μm for which the net value is zero, and beyond which the FW50 value increases again. This change trend of FW50 blur is due to the $|A_3|$ change as a function of Δr. To better understand this behavior of A_3, the characteristic function, $\phi_4(z)$ for five different values of Δr is also shown in the inset figure. Eq. (5) indicates that the A_3 coefficient and accordingly the FW50 value of the blur due to
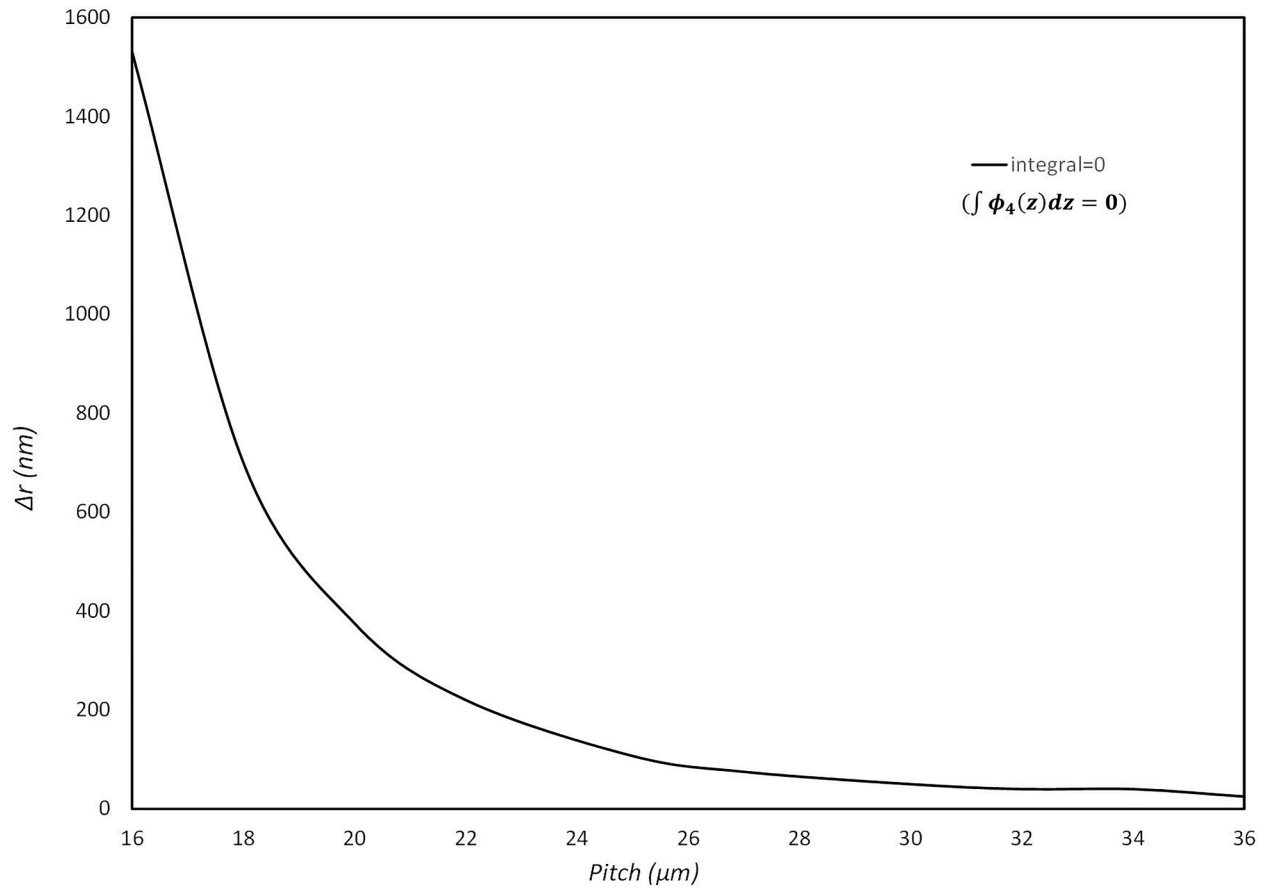
Fig. 13. The relationship between the Δr for which $\int \phi_4(z)dz = 0$ and the pitch between the apertures. The electric field on the ALA was the nominal value of 2.13 kV/mm. why Figure 7 has appeard on top of this figure? it shouldn't be here.
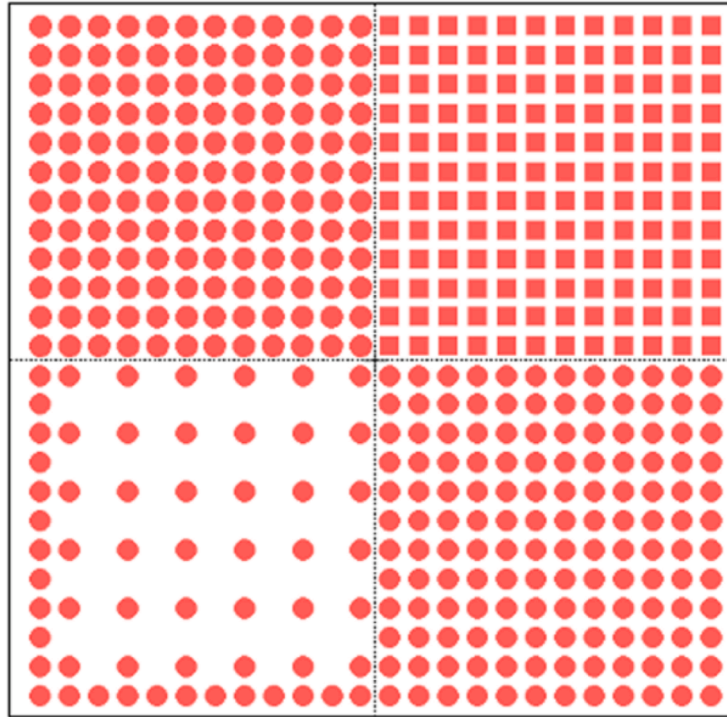
Fig. 14. ALA layout with four different quadrants, each having its own aperture shape and layout, as described in the main text.
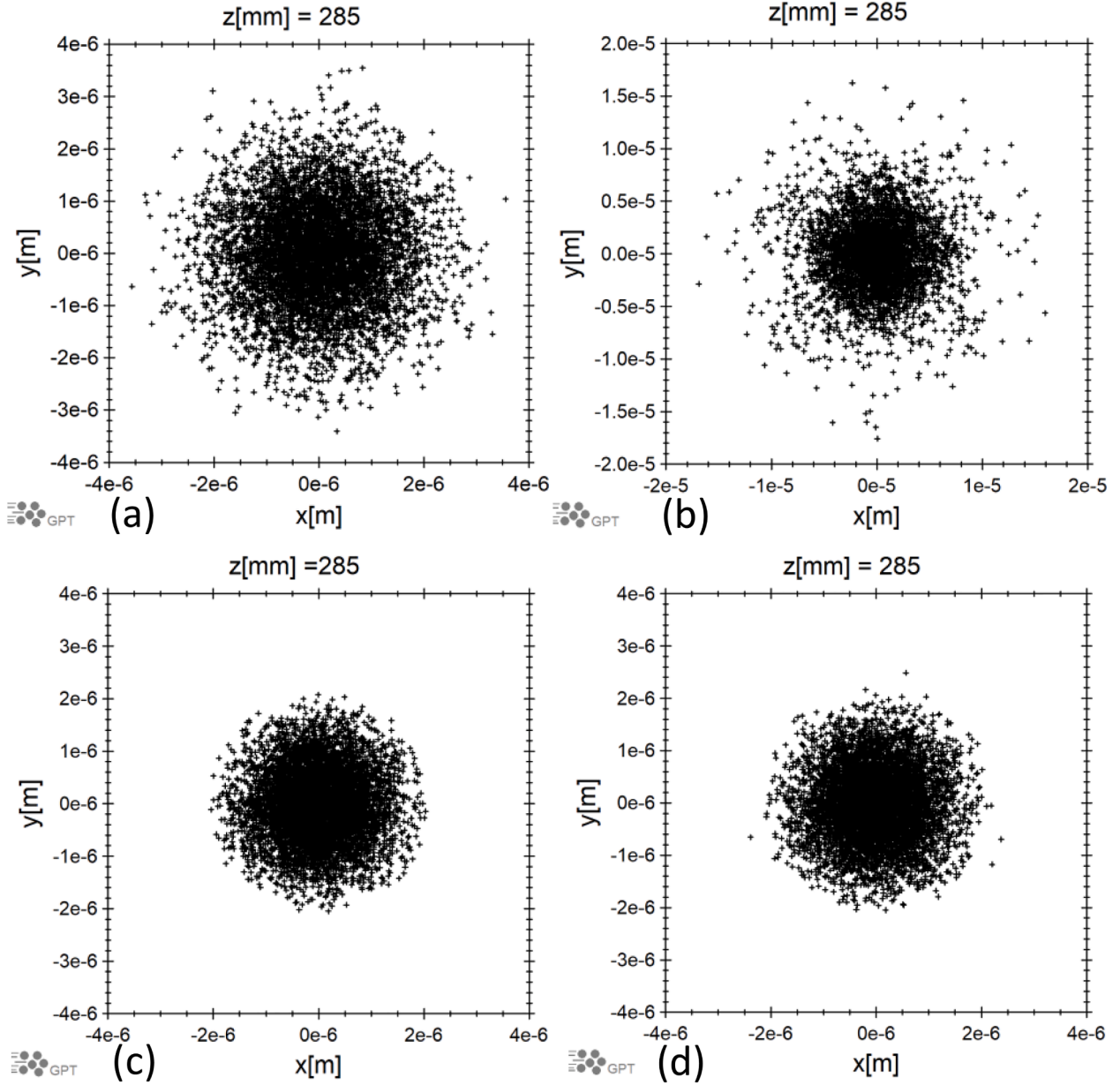
Fig. 15. Simulated spot profiles at the MBS image plane for an axial (central) micro-aperture lens with eight neighbouring aperture lenses having a) regular round shape; b) rounded square shape with Δr=1.4 µm; c) round shape, with double pitch; d) rounded square shape with optimum Δr=0.4 µm. Note that the scale of panel b is different. The FW50 size of the spot in panel c is 1.6 µm which is equal to the size of the spot in Fig. 3b indicating that by doubling the pitch the neighbouring octupole effect disappears completely. The FW50 size of the spot in panel d is 1.77 µm. This confirms that in the simulated configuration, the counteracting octupole effect from rounded square aperture lenses with $\Delta r = 0.4$ µm suppresses the neighbouring octupole effect greatly.

the octupole effect is directly proportional to the area under each $\phi_4(z)$ graph ($\int \phi_4(z)dz$). For regular, round apertures the area under this function is a (large) positive value and so is A_3. For increasing values of Δr, there is an increasing counteracting negative octupole contribution leading to a reduced area under the curve. At Δr=0.372 µm the net area under the curve is close to zero, and beyond that the value of the counteracting negative octupole takes over, leading to a larger (negative) area under the curve, and hence a larger $|A_3|$ value. Although the value of $\int \phi_4(z)dz$ depends linearly on the electric field on the ALA, the Δr for which $A_3 = 0$ ($\int \phi_4(z)dz = 0$) is independent of this field as shown in Fig. 12. On the other hand, the Δr for which $A_3 = 0$ does depend strongly on the pitch, as shown in Fig. 13. This is in good agreement with the results presented by Roelofs and Barth [11].

To experimentally validate the prediction that rounded square apertures with $\Delta r = 0.4 \mu$m can be used to eliminate fourfold astigmatism,

we have designed a dedicated ALA with four different quadrants as shown schematically in Fig. 14. Each quadrant has its own aperture shape and layout. The top left quadrant is filled with regular, round apertures of 15 µm diameter and with 20 µm pitch as a reference. The bottom left quadrant has twice the pitch (40 µm), which should serve to very effectively minimize the octupole effect, but at the cost of unacceptable reduction of transmitting beam through it. We include it as a benchmark for the final spot size. The bottom right quadrant is filled with rounded square apertures of 15 µm diameter, 20 µm pitch and $\Delta r = 0.4$ µm as calculated to be close to the optimum. Finally, the top right quadrant is filled with rounded square apertures of 15 µm diameter, 20 µm pitch and $\Delta r = 1.4$ µm. This should result in an enhanced, and hence more clearly visible octupole effect, but opposite to the original effect in the uncorrected ALA. Before turning to experimental results, in the remainder of this section we will look more closely into ray tracing
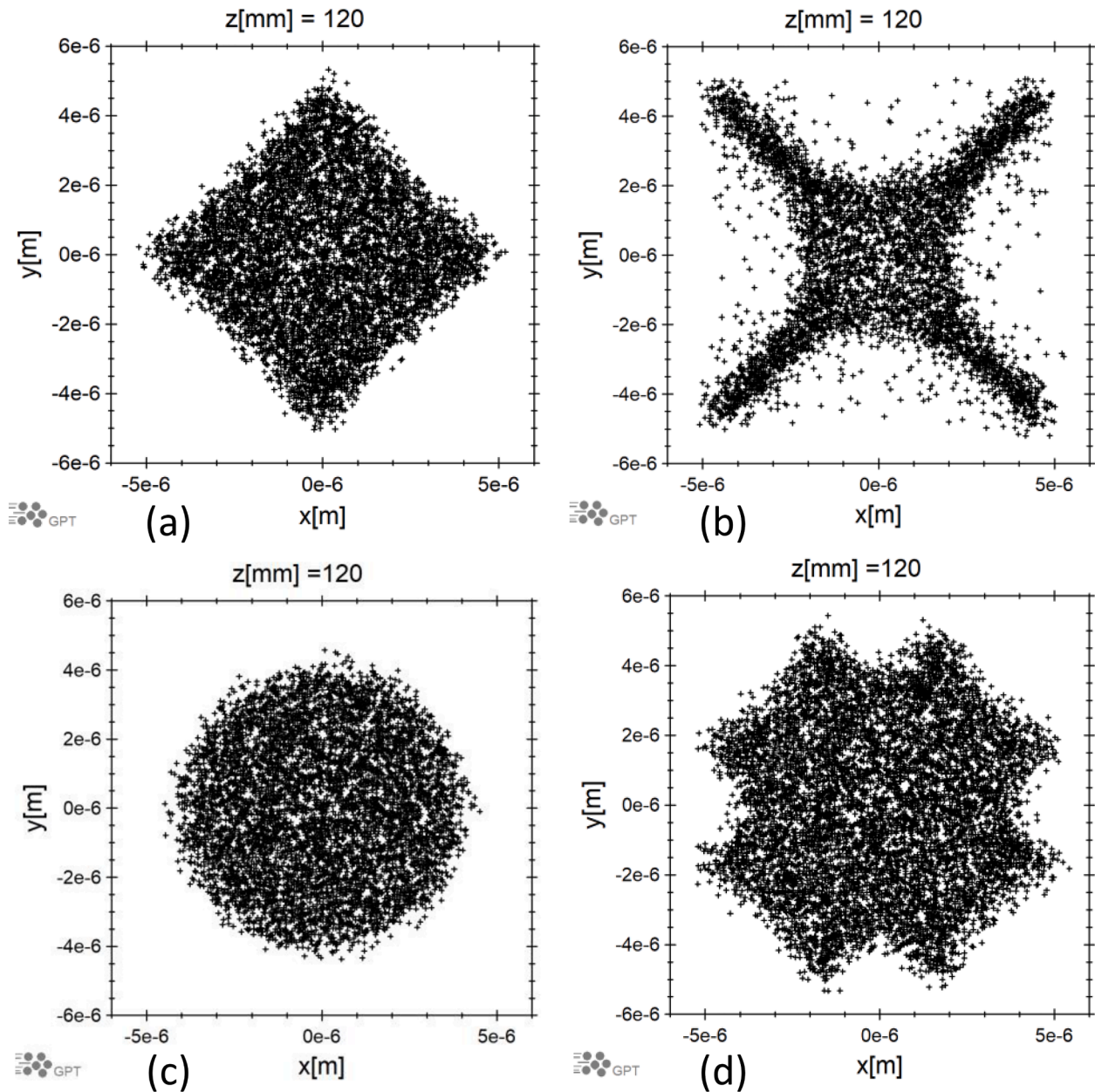
Fig. 16. Simulation results of under-focus spots for the same aperture shapes as in Fig. 15.

simulation results for this particular ALA geometry.

An ALA with four different quadrants cannot be simulated in a single simulation run due to a limited computational budget, as explained in Section 2.1. Hence, every quadrant was simulated separately. Moreover, in every simulation only a subset of 3 × 3 apertures, central aperture lens with eight neighbouring aperture lenses, was used and the particles were only traced through the central aperture lens. The results of these separate simulations are summarised in Fig. 15 for the in-focus plane. In each of the panels a (focused) spot profile is recorded at the MBS image plane for an aperture lens from one of the four different quadrants of the ALA – top left quadrant (a), top right quadrant (b), bottom left quadrant (c), and bottom right quadrant (d).

The FW50 size of the spot in Fig. 15c is 1.6 μm, which is equal to the size of the spot in Fig. 3b for an aperture without neighbours. This demonstrates that by doubling the pitch, the neighbouring octupole effect is indeed substantially eliminated as it was expected from Fig. 6. Fig. 15b and d show the (focused) spot profile at the MBS image plane for an axial (rounded square) micro-aperture lens with eight

neighbouring micro-aperture lenses with Δr =1.4 and 0.4 μm, respectively. The FW50 size of the spot in Fig. 15d is 1.77 μm, demonstrating that the octupole effect is compensated to a great extent. This result is also in a reasonably good agreement with analytically calculated blurred spot size from the data presented in Fig. 11 where the blur is added quadratically to the (virtual) object size. Fig. 15b shows that the counteracting octupole effect is overdone for Δr =1.4 μm; the focused spot is clearly enlarged compared to all other spots – note the different scale for this spot.

The residual octupole effects in the beams can be clearly seen in the spot profiles recorded at a relatively large under-focus plane. Fig. 16 shows the spots at positions $\Delta z = -100$ mm before the focus plane, for the same four aperture shapes as in Fig. 15. It is interesting to see that the counteracting octupole effect for apertures with Δr=1.4 μm (Fig. 16b) clearly overcompensates for the original octupole effect. This can be understood by comparing the orientation of the fourfold shape of Fig. 16b to that of the uncorrected aperture shape in Fig. 16a. Moreover, from Fig. 16d, it is clear that the Δr=0.4 μm aperture shape is effective at
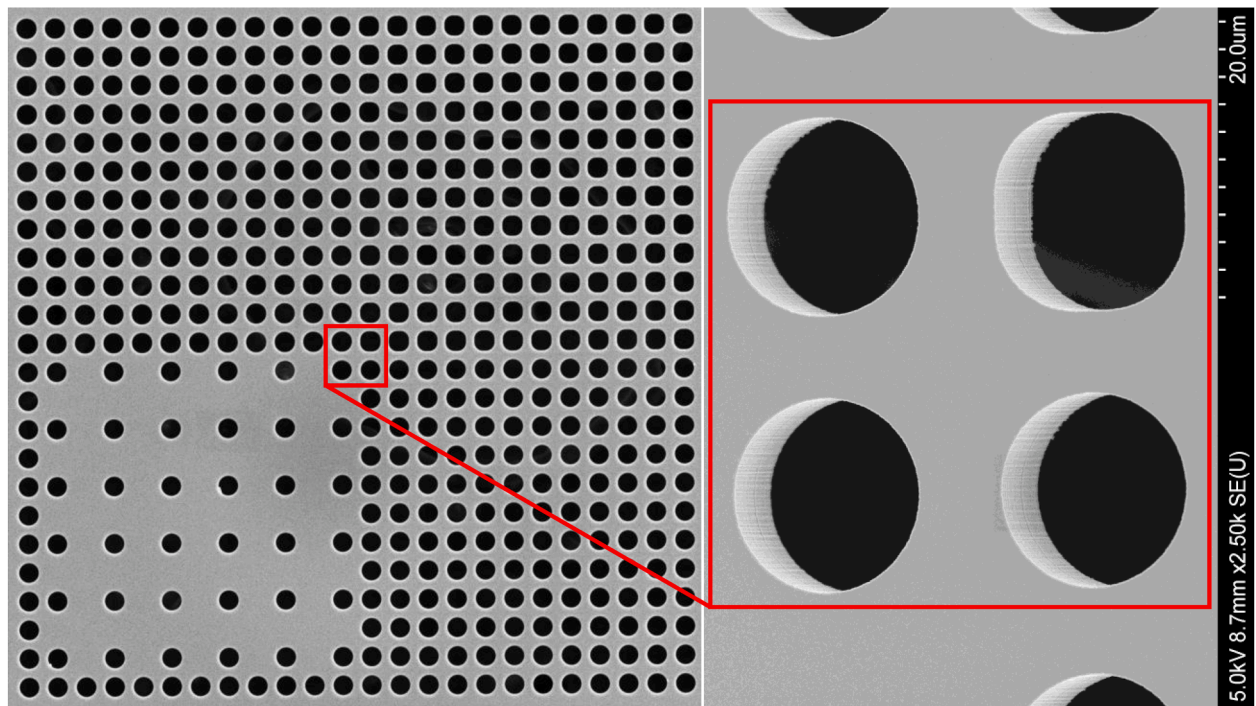
Fig. 17. Low and high magnification SEM image of the new ALA with four different quadrants according to the design of Fig. 14.
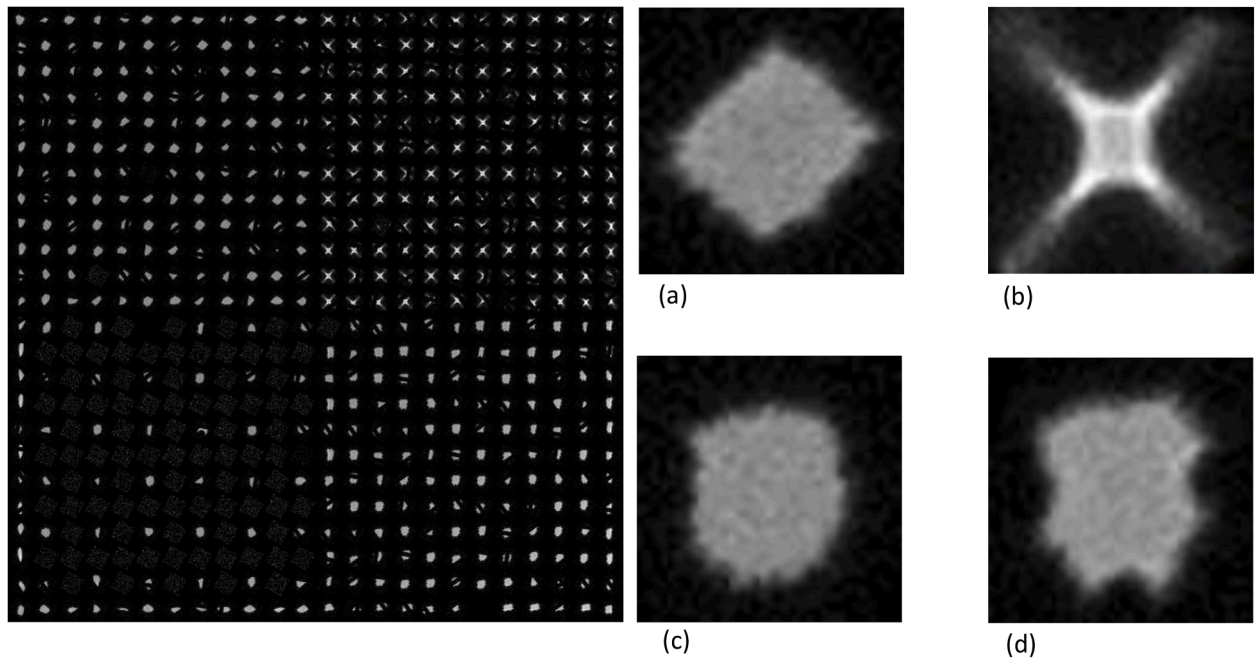

Fig. 18. Typical under-focused spots of the MBS on the YAG screen (left). To produce this image, all the electrodes of the MBS are set to the voltages for producing focused spots at the screen, except the focusing electrode (E-1) of which the voltage is set 1% lower. To produce this image, we recorded the images of the individual spots separately, and then stitched them together in post-processing. Many of the spots are partly hidden behind a line pattern that was deposited on the YAG for other purposes. Individual under-focused spot images (a-d) are selected because of their similarity to the spot profiles shown in Fig. 16 (a-d).

eliminating the octupole effect. However, it also shows that inevitably the next higher-order aberration now becomes the dominant one, which given the symmetry of the ALA is a 16-pole effect, leading to an eightfold star shape. However, as said above, by comparing the FW50 sizes of the focused spots in Figs. 15c and 15d, one can conclude that although the 16-pole effect is clearly visible, it does not contribute nearly as much to the (in-focus) spot size as the uncorrected octupole effect does.

4.3. Experiment results and discussion

In the experimental setup shown in Fig. 7, the ALA of the MBS was replaced with a new ALA according to the design of Fig. 14. An SEM image of the new ALA with four different quadrants is shown in Fig. 17.

As mentioned earlier, the octupole effect can be seen most clearly at the under- or over-focus planes. Fig. 18 shows typical under-focused
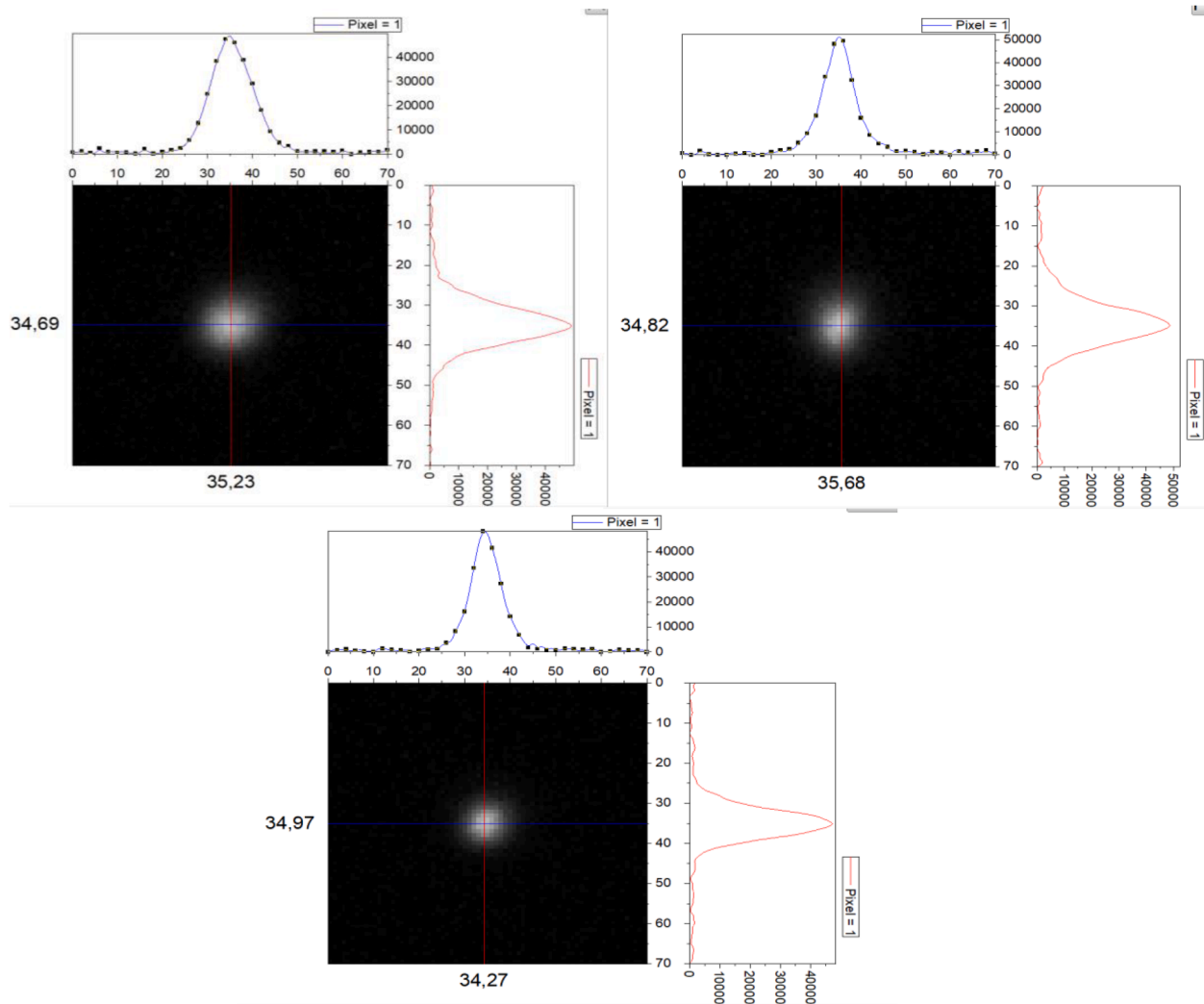
Fig. 19. Three typical MBS focused spot images on the YAG screen. Panel a, from the top left quadrant (regular apertures); panel b, from the bottom right quadrant (rounded square apertures with $\Delta r =0.4$ µm); panel c, from the bottom left quadrant (regular apertures with a doubled pitch).

spots of the MBS on the YAG screen. As noted, in Section 3.2, in the experimental setup the position of the YAG screen is fixed. Rather, starting from a focusing condition, an under-focus plane was brought to the YAG screen by reducing the E-1 Vage by 1% from its nominal value. To produce this image, we recorded the images of single spots individually, and then stitched them together to represent the full array. Panels a-d of Fig. 18 show examples of spots from each of the different quadrants. They are, in fact, the closest experimental realization of the simulated spot profiles as shown in Fig. 16 (a-d).

The experimental results presented so far are in a reasonably good qualitative agreement with those predicted by simulations. Next, we turn our attention to checking how the results of simulation and experiments agree quantitatively, by comparing the sizes of the focused spots at the screen. Fig. 19 shows three typical MBS focused spot images on the YAG screen. These direct CCD images are taken from selected focused spots from three different quadrants of the ALA – for the regular apertures, the rounded square apertures with $\Delta r =0.4$ µm, and the regular apertures with a doubled pitch. To produce these images, we set the electrode voltages of the MBS to the optimum (nominal) values for minimum beam sizes in the top left quadrant. Intensity profiles of these spots are shown for lines going through the centers of mass of these spots in x (blue line) and y (red line) directions. Horizontal scales in the profiles are in units of pixels, where the pixel size corresponds to 360 nm on the YAG screen. From these profiles, FWHM spot sizes in x and y

Table 1

measured spot sizes for regular apertures (TL), optimized rounded-square apertures (BR) and double-pitch regular apertures (BL).

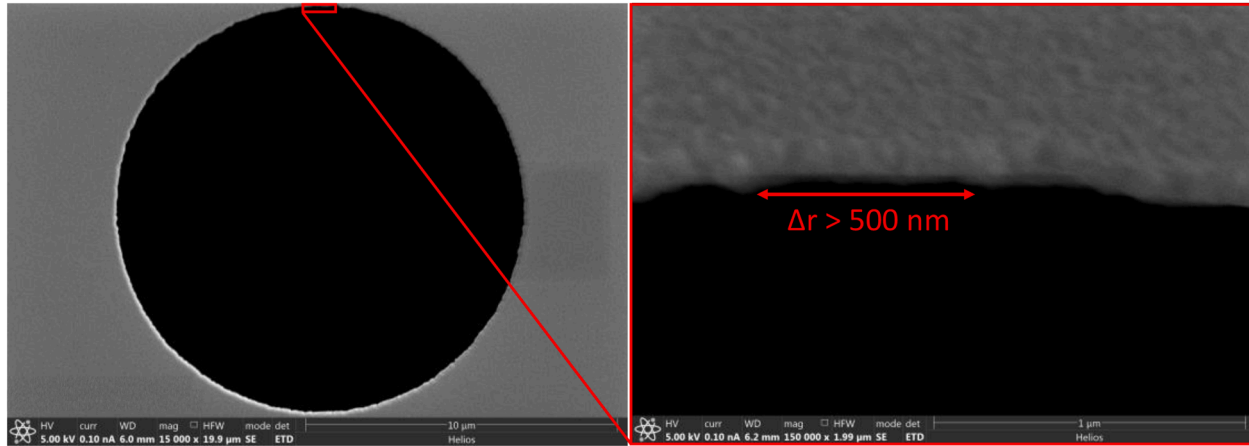| size/quadrant	TL	BR	BL
FWHM_X (µm)	3.31	2.54	2.38
FWHM_Y (µm)	3.08	3.2	2.3
Average_FWHM (µm)	3.2	2.87	2.34

directions have been derived, as summarized in Table 1.

The average spot size for the regular apertures in the top left quadrant (TL) is 3.2 µm, for the rounded-square apertures in bottom right quadrant (BR) it is 2.85 µm, and of the doubled-pitch apertures in bottom left quadrant (BL) it is 2.34 µm. The theoretically predicted beam size, including the contributions from the geometric source image, axial aberrations, four-fold astigmatism and electron diffraction for TL, BR and BL is 2.74 µm, 1.9 µm and 1.76 µm, respectively. We first note that all of the measured spot sizes are somewhat larger than their simulated counterparts. There are multiple reasons for this. Due to the typical diffraction limitation of the light optical setup, the smallest beam size we could measure in the setup was 2 µm. Hence, to obtain the real spot sizes, the measured ones would need to be deconvoluted with the resolution of the optical system. In addition, all of the spots seem to contain some twofold astigmatism as apparent from the different sizes in x and y

Table 2

DF values as defined in the main text. Simulated spot sizes that are below the measurement resolution are marked with an asterisk (*) and replaced by a value of 2 μm for the purpose of the adjusted DF calculation.

|		TL	BR	BL
Spot sizes [μm]	Experiment	3.2	2.87	2.34
	Simulation	2.74	1.9*	1.76*
Deviation factors (DF)	Measured	1.17	1.5	1.33
	Adjusted	1.17	1.44	1.17

expected. A reduced field on the surface of the ALA also changes the total spot blur contribution from four-fold astigmatism, but only marginally. As can be derived from Fig. 12, the value of $\int \phi_4(z)dz$ depends linearly on the field on the ALA. Considering that the nominal Δr used in the experiment (of 0.4 μm) is very close to its optimum value (=0.372 μm), a smaller field should have led to a very marginal change in overall octupole effect. However, as noted above, upon closer inspection in the SEM it was found that the actually realized rounded-square shapes showed significant deviations from the design. The di-

Fig. 20. SEM image of one of the rounded-square apertures. The Δr is larger than expected, and the diameter of the aperture is 1 μm smaller than expected.

directions, which can be partially due to off-axial astigmatism, as they are all off-axis with respect to the common optical axis of the MBS. Finally, Coulomb interactions were not included in the simulations, but are known to affect experimental spot sizes at higher beam currents, as mentioned in Section 1.2. These enlarged experimentally measured spot sizes shouldn't be a problem if the deviation is "similar" for spots in different quadrants. To show the difference more clearly, we define a deviation factor (DF) for each quadrant as the ratio between experimentally measured spot size to the simulated spot size of that quadrant. Table 2 shows the DFs between the simulated and the measured spots listed in the row labeled as "measured". However, as mentioned earlier, the resolution of our spot measuring setup is 2 μm. We account for this by setting a minimum of 2 μm for the simulated spot sizes. This results in a set of new (expected) DF values as listed in Table 2 under the name "adjusted". The DF values for the TL and BL quadrant are now the same, whereas for the BR quadrant, there is a significant deviation of about 23% with respect to the others. This difference is significant and needs to be explained.

From the numbers in Table 1 it is clear that the rounded-square apertures with Δr=0.4 μm effectively appear to correct the fourfold astigmatism to a great extent, as the measured spot size is smaller than the one for regular apertures. However, from DF values of Table 2 we also note that the correction is not as effective as expected from simulations. Now the question is, can this relatively large difference of DF between BR and two other quadrants be explained? The short answer is yes. To elaborate, upon closer inspection we have found two discrepancies in our experiment compared to the nominal design. First, we found that the voltage of the E-2 electrode was 6.5% lower than the nominal value as used in simulations, due to a flaw in reading off the power supplies. This led to a weaker electric field on the ALA by a similar fraction. Second, upon closer inspection in SEM, we found that the rounded-square aperture sizes and shapes exhibit some deviations compared to the design. Those deviations will be discussed in further detail below. Starting with the reduced field on the surface of the ALA, it could lead to a larger magnification of the spots on the YAG screen, which could be another reason why all measured spots were larger than

ameters of the apertures in the BR quadrant were only 14 μm instead of 15 μm. Also, the Δr values were much larger (by >100 nm) than the intended ones, and not well controlled along different sides of the aperture; see the SEM images in Fig. 20. Smaller diameter apertures with a larger Δr will introduce a much larger counteracting octupole.

To study the effect of these experimental deviations from the simulated shapes, a new set of simulations were carried out where all these observed deviations were applied to the electrode potentials and the geometry of the ALA. Figs. 21a-d show the spot profile at the MBS image plane for an axial aperture lens with eight neighboring aperture lenses having a) rounded square shape with Δr=0.5 μm, 6.5% weaker field on the ALA and 14 μm aperture diameter (as realized in our experiment); b) rounded square shape with Δr=0.4 μm and nominal field on the ALA and nominal aperture diameter (as intended); c) regular aperture with 6.5% weaker field on the ALA, and d) regular aperture with nominal conditions. The FW50 size of the spot in panel a is 2.27 μm, whereas in panel b it is 1.77 μm, which is equal to the size of the spot in Fig.15d The FW50 sizes of the spots in panels c and d are almost the same, indicating that 6.5% weaker field on the ALA does not change the magnification noticeably. The expected total beam size, including the contributions from the geometric source image, axial aberrations, four-fold astigmatism and diffraction[1] for the spot in panel a add up to 2.43 μm. With this new simulation result, the "expected" DF value for the BR quadrant decreases from 1.44 to 1.18, which is very close to 1.17 for other two quadrants.

Fig. 22 shows the octupole characteristic function, $\phi_4(z)$, for four different possible cases: 1) (black solid line) for ideal regular apertures with 15 μm diameter and a nominal field on the ALA, 2) (red dotted line) for the same ideal regular apertures with 15 μm diameter, but with a 6.5% weaker field on the ALA as in the experiment, 3) (green solid line) for rounded-square apertures with Δr=0.4 μm, 15 μm diameter and a nominal field on the ALA (ideal condition), 4) (blue solid line) for

---

[1] Due to a smaller aperture size, FW50 size of diffraction is increased to 0.36 μm.
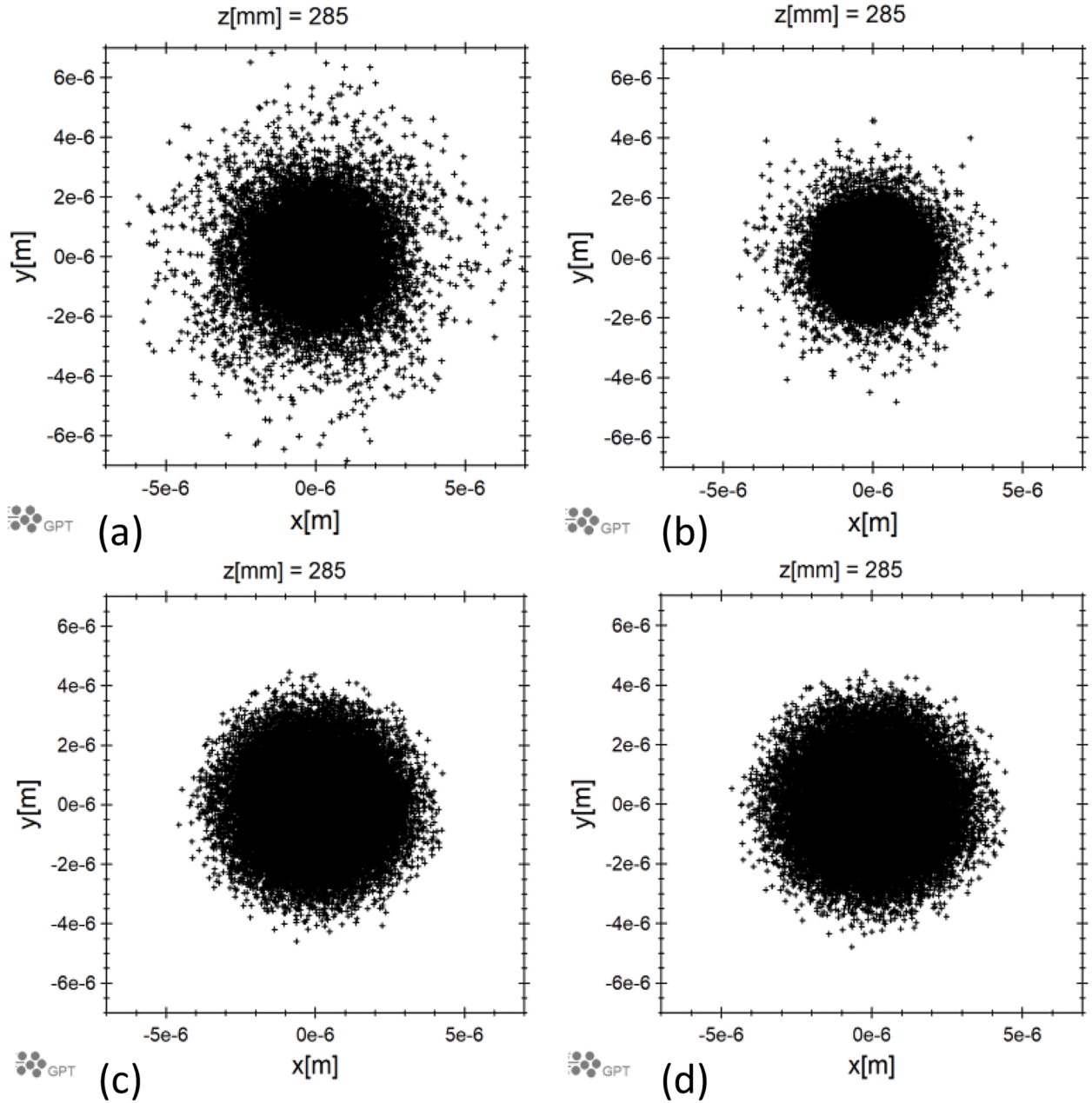
Fig. 21. Simulated spot profiles at the MBS image plane for an axial (central) micro-aperture lens with eight neighbouring aperture lenses having a) rounded square shape with Δr=0.5 μm, 6.5% weaker field on the ALA and 14 μm aperture diameter; b) rounded square shape with Δr=0.4 μm and nominal field on the ALA and nominal aperture diameter; c) regular aperture with 6.5% weaker field on the ALA and d) regular aperture with nominal conditions. The FW50 size of the spot in panel a is 2.27 μm, while in panel b it is 1.77 μm, which is equal to the size of the spot in Fig. 15d. The FW50 sizes of the spots in panels c and d are almost the same, indicating that 6.5% weaker field on the ALA does not change the magnification noticeably.

rounded-square apertures with Δr=0.5 μm, a smaller diameter of 14 μm, and with a 6.5% weaker field on the ALA, closer to what is basically used in the experiment. From the two graphs for regular apertures, it can be concluded that a 6.5% weaker field on the ALA, has indeed an small effect on $\phi_4(z)$, for regular round apertures. On the other hand, the blue solid curve representing $\phi_4(z)$ for the experimental condition for rounded-square apertures of the bottom right quadrant, shows a considerable difference compared to the nominal case as represented by the green solid curve. Stated differently, for optimized rounded-square apertures in the ideal situation, $\int \phi_4(z)dz$ is close zero whereas, due to the deviations in the ALA conditions used in the experiment, the integral under the blue solid curve has now become negative and relatively large. The residual opposite octupole effect enlarges the spot size significantly.

This explains the relatively large discrepancy of about 23% in the DF between BR and other quadrants as presented in Table 2. The inset figure also shows the analytically calculated FW50 sizes of the octupole blur at the object. As can be seen, the FW50 blur added to the object from condition (4) is about 65% of that of the non-corrected ideal condition. In fact, the deviated condition imposes a counteracting octupole effect that has FW50 blur addition to the object of about 65% of the non-corrected condition and that explains why the DF value for BR is 23% larger than the other quadrants.

5. Conclusions

It was found, from the simulation results as presented in this work,
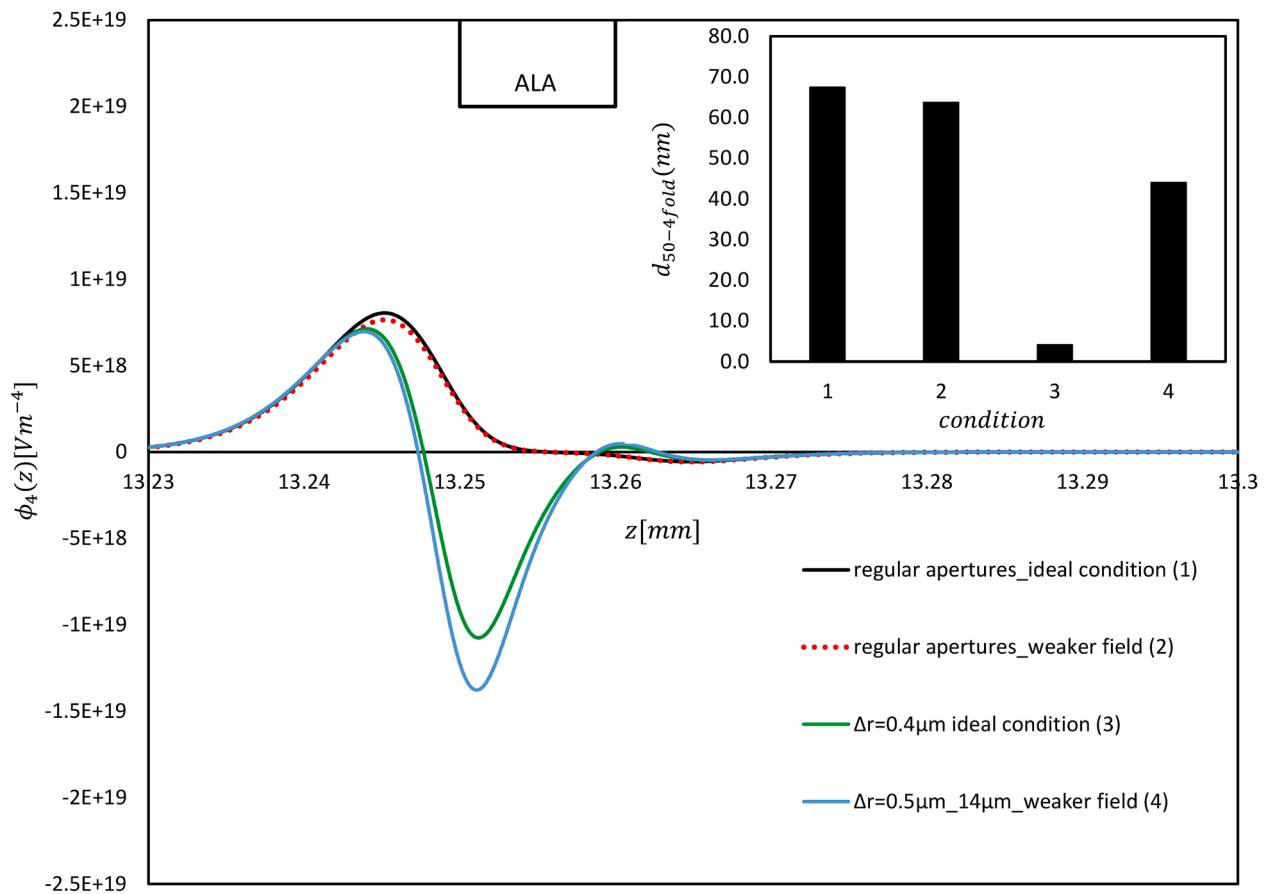
Fig. 22. The octupole characteristic function, $\phi_4(z)[Vm^{-4}]$, for different simulated cases, as described in detail in the main text. From this figure, the area under these graph ($\int \phi_4(z)dz$) can be determined to represent the net octupole effect in each case (see inset). This demonstrates why the counteracting octupole effect by rounded-square micro-aperture lenses as in our experimental realization, suppresses the neighbouring octupole effect greatly, though not fully.

that for MBSEM ALAs, *neighbours indeed matter.* By comparing the spot sizes for the beams with and without neighbours, it was found that the fourfold astigmatism effect caused by the neighbouring apertures could enlarge the spot sizes of the array of focused beams. The observations were subsequently confirmed experimentally, in particular by inspecting spot shapes in out-of-focus planes. Similar simulations have led us to propose a mitigation of the effect by introducing a non-roundness to the aperture shapes. The solution was again confirmed experimentally, this time through use of a dedicated setup and a four-quadrant ALA specifically designed for the purpose. However, the experimental validation of our proposed solution has also demonstrated that careful control over the aperture dimensions, the detailed shape of the perimeter, and to a lesser extent the various electrode voltage, is crucial for optimal performance of the MBS.

Declaration of Competing Interest

Based on the Delft MBSEM, Thermo Fisher and DELMIC produce the FAST EM. AMG and EK are employed by Thermo Fisher, PK is co-founder of DELMIC.

Data Availability

Data will be made available on request.

Acknowledgments

WE would like to thank Carel Heerkens and Martin Kamerbeek for

References

[1] A.L. Eberle, S. Mikula, R. Schalek, J.W. Lichtman, M.L. Knothe Tate, D. Zeidler, High-resolution, high-throughput imaging with a multibeam scanning electron microscope, J. Microsc. 259 (2) (2014) 114–120.

[2] A. Mohammadi-Gheidari, C.W. Hagen, P. Kruit, Multibeam scanning electron microscope: experimental results, J. Vac. Sci. Technol. B 28 (6) (2010) C6G5–C6G10.

[3] A. Mohammadi-Gheidari, P. Kruit, Elecron optics of multi-beam scanning electron microscope, Nucl. Instrum. Methods A 645 (1) (2011) 60–67.

[4] A. Mohammadi-Gheidari, in a Scanning Electron Microscope, Delft University of Technology, Delft, 2013, p. 196 Beams.

[5] Y. Ren, P. Kruit, Transmission electron imaging in the Delft multibeam scanning electron microscope1, J. Vac. Sci. Technol. B 34 (6) (2016).

[6] Y. Ren, Imaging Systems in the Delft Multi-Beam Scanning Electron Microscope1, Delft University of Technology, Delft, 2017.

[7] W. Zuidema, Y. Ren, J. Hoogenboom, C.W. Hagen, P. Kruit, Transmission imaging of biological tissue with the Delft multi-beam SEM, European Microscopy Congress 2016 Proceedings, Am. Cancer Soc. (2016) 394–395.

[8] Y. Zhang, P. Kruit, Design of a high brightness multi-electron-beam source, Phys. Proc. 1 (1) (2008) 553–563.

[9] Y. Zhang, A 100-Electron-Beam Source from a High Brightness Schottky Emitter For Fast Patterning Applications, Delft University of Technology, Delft, 2008.

[10] http://www.lencova.com/index.php/about-eod.

[11] B.J.G.M. Roelofs, J.E. Barth, Feasibility of multi-beam electron lithography, Microelectron. Eng. 2 (1984) 259–279.

[12] R. Knippelmeyer et al., US 2017/0287674 A1.

[13] http://www.pulsar.nl/gpt.

[14] J. Barth, P. Kruit, Optik (Stuttg) 101 (3) (1996) 101.

[15] L.A. Baranova, S.Y. Yavor, F.H. Read, Crossed aperture lenses for the correction of chromatic and aperture aberration, Rev. Sci. Instrum. 67 (3) (1996) 756–760.